CFD-based development, testing and optimization of flat plate collectors

Beate Vetter, Stephan Fischer, Harald Drück

University of Stuttgart, Institute for Building Energetics, Thermotechnology and Energy Storage (IGTE)[1], Stuttgart (Germany)

Abstract

Based on CFD (Computational Fluid Dynamics) simulations and virtual thermal performance tests, a development and optimization tool for flat plate collectors is presented. Using the example of a serial product flat plate collector, parametrized CAD data were generated. Dimensions like length, width and thickness of the transparent cover or the dimensions of the pipes, the aperture area and the welding lines are parametrized. Therewith geometrical changes can be executed quickly at a later stage for optimization. Essential for simulating solar collectors is the radiation spectrum model. The Multiband Thermal radiation model was chosen. It allows specifications of user-defined spectral bands, for which optical properties of the surfaces are defined. Thereby implementation of selective absorber coating is possible. Using a heat transfer coefficient, convection to the environment is taken into account by implementation as a boundary condition. Literature shows a wide range of convective heat transfer coefficients for forced air over flat surfaces, particularly flat plate collectors, which are based on empirical examinations and from boundary layer theory. Taking into account, that virtual dimensions of the collector are variable, selection of an equation from boundary layer theory is shown. Finally, results from a virtual thermal performance test are presented. Simulated component temperatures and peak collector efficiency from the virtual thermal performance test correspond well to measured values. With increasing mean fluid temperature, the difference between measured and simulated outlet temperature rises. Possible reasons are identified and presented.

Keywords: virtual thermal performance test, flat plate collector, CFD (Computational Fluid Dynamics)

1. Introduction

Knowledge of the thermal performance of the collector is required for the prediction of the energy output of a solar thermal system. Thermal performance test procedures are e.g. defined in **DIN EN ISO 9806:2017**. In phases of new and further development as well as for the optimization of flat plate collectors, the knowledge of the thermal performance as well as component temperatures such as the maximum temperature of the thermal insulation, are of interest before building and physically testing a prototype. To achieve this goal a CFD-based development and optimization tool, including a virtual thermal performance test procedure for flat plate collectors, is being developed in the VirtColl+ project. The paper presents the methodical approach and simulation results using the example of a serial product flat plate collector.

The CFD calculation is based upon modeling the physical processes in and around the flat plate collector. Therefore, in the first step, flat plate collectors are implemented in a CFD program and the outlet temperature as well as the component temperatures are calculated depending on the ambient and operating conditions (e.g. mass flow rate, inlet temperature, etc.) and the collector's construction (e.g. type of absorber coating, type and thickness of thermal insulation material, etc.). Due to specific ambient and operating conditions, the collector's performance can be virtually determined in a second step. On the basis of the virtually created measurement

[1] On July 1, 2018 the Institute for Building Energetics (IGE), the Institute of Thermodynamics and Thermal Engineering (ITW) with its Research and Testing Centre for Thermal Solar Systems (TZS) as well as the Institute of Energy Storage (IES) have been merged to the Institute for Building Energetics, Thermotechnology and Energy Storage (IGTE)

doi:10.18086/eurosun2018.12.03 Available at http://proceedings.ises.org

data generated by means of CFD simulations, the conventional collector parameters are determined via parameter identification in an established way, compliant with standard. The paper shows the methodical approach from CAD data buildup to validation by means of a stationary thermal performance test of a serial product flat plate collector. During the thermal performance test, component temperatures were also measured.

The advantage of a CFD-based development, is the possibility to analyze a plurality of parameter alternatives in the forefront of prototyping. The CFD software used is STAR CCM+.

2. Environment and operating conditions for stationary thermal performance tests according to DIN EN ISO 9806

One collector was equipped with thermocouples on the absorber and the frame to validate the component temperatures resulting from the simulations. This collector was tested indoor in a solar simulator (collector C1375). In addition, another collector of the same type equipped with only a single thermocouple on the absorber was tested in- and outdoors (collector C1373). The efficiency curves are shown in Fig. 1. Instantaneous collector efficiency is calculated according to Eq. 1.

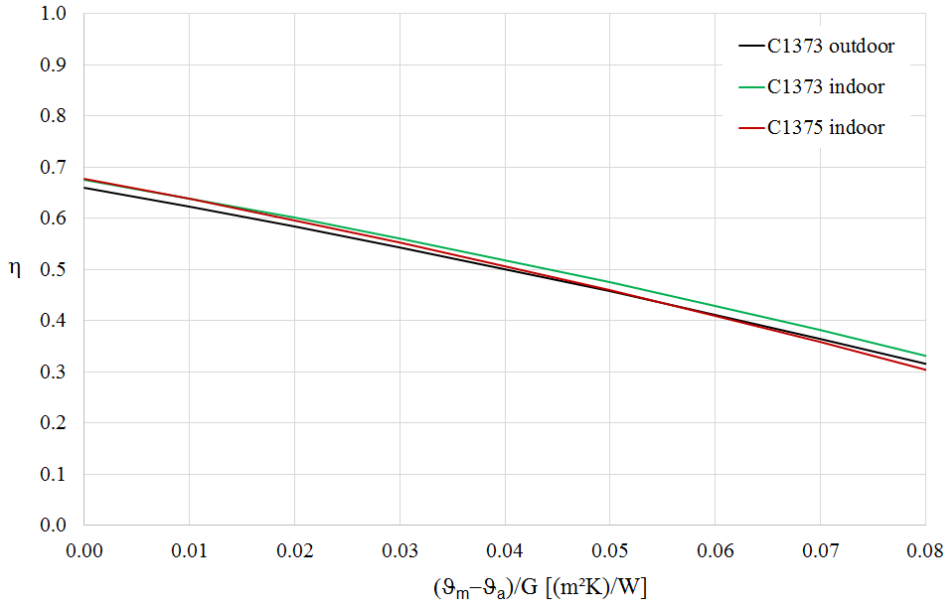

Fig. 1: Efficiency curves for stationary thermal performance test of collectors C1373 and C1375

$$\eta = \frac{\dot{m} * c_p * (\vartheta_{out} - \vartheta_{in})}{A * G} = \eta_0 - a_1 * \left(\frac{\vartheta_m - \vartheta_a}{G}\right) - a_2 * \left(\frac{(\vartheta_m - \vartheta_a)^2}{G}\right) \quad \text{Eq. 1}$$

with:

η	instantaneous collector efficiency	[-]
$\dot{m}$	mass flow rate	[kg/s]
c_p	specific heat capacity	[J/(kg K)]
ϑ_{out}	collector outlet temperature	[°C]
ϑ_{in}	collector inlet temperature	[°C]
A	gross collector area	[m²]
G	hemispherical solar irradiation	[W/m²]
η_0	peak collector efficiency	[-]
a_1	heat loss coefficient at (ϑ_m - ϑ_a) = 0	[W/(m² K)]
a_2	temperature dependence of the heat loss coefficient	[W/(m² K²)]
ϑ_a	ambient temperature	[°C]
ϑ_m	mean temperature of heat transfer fluid	[°C]

Collector parameters η_0, a_1 and a_2 are identified from measurement results by parameter identification.

Comparing the indoor measurement results of C1373 and C1375 the following can be observed:

- The efficiency curve of C1375 shows a slightly larger gradient than the efficiency curve of C1373 which indicates higher thermal losses with increasing mean fluid temperature. Possible explanations are series scattering, minor defects due to the installation of the thermocouples and measurement uncertainties.
- The η_0 of the outdoor test (C1373) is lower compared to indoor test (C1375). This is not exceptional and in a range which is not uncommon as solar simulators usually do not match solar spectrum to 100 %.

Component temperatures of the CFD simulation are validated with the temperatures measured during the thermal performance test of C1375 in the solar simulator. Therefore, environment and operating conditions from this measurement were implemented as boundary conditions in the simulations, compare Tab. 1.

Tab. 1: Thermal performance test C1375, environment and operating conditions

Mass flow rate	0.042 kg/s
Inlet temperatures	19.9 °C, 40.8 °C, 60.3 °C, 79 °C
Wind velocity	2 m/s; (3 m/s C1373 outdoor)
Ambient temperature	22 °C
Hemispherical solar irradiation	788 W/m²

3. CAD buildup and meshing

CFD-based development always starts with CAD (computer-aided design) data. Either available CAD data is imported in the CFD software or parameterized CAD data of the collector, more suitable for parameter studies, are prepared. Fig. 2 shows an isometric mapping of the collector in transparent mode. Fig. 3 illustrates a sectional drawing through a part of the collector geometry. The collector's gross area is 2.1 m². The absorber is a selective coated aluminum sheet with copper pipes; the flow pattern is a harp with eight riser pipes. The bonding between the absorber sheet and piping is done by ultra-sonic welding. CAD data were prepared and parameterized using the 3D CAD tool included in STAR CCM+. Dimensions like length, width and thickness of the frame, transparent cover, absorber and the thermal insulation as well as the dimensions of the pipes, the aperture area and the welding line are parametrized and thereby can be changed quickly at a later stage for performance optimization. The advantage of preparing the CAD data in the same tool where the CFD calculations are done, is that the preparation and manipulation of the CAD data can be done without editing surface classifications after changing dimensions. The interface between transparent collector cover and ambient for example remains the same for all defined optical properties and boundary conditions after enlargement or reduction the aperture area in size.

Fig. 2: Isometric collector mapping (transparent mode)

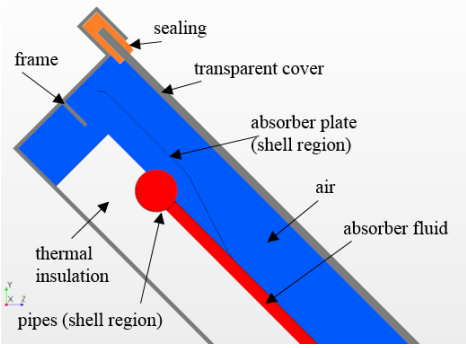

Fig. 3: Sectional drawing through part of the collector geometry

Beate Vetter

One challenge in buildup and meshing a flat plate collector is, that the dimensions differ in the range of meters for horizontal dimensions (length and width of the transparent cover, the thermal insulation etc.) and in the range of some tenths of a millimeter for material thicknesses (absorber plate, pipes). Meshing such thin solids is not practical and leads to an enormously large number of cells. Therefore, the Shell Three-Dimensional model is used for the absorber plate and the absorber pipes. This model represents a volume in space whose thickness is so small that it can be adopted as a surface with a single-cell thickness in the normal direction. Instead of building the pipes as a volume for example, only the water in the pipes is created in the first step. A shell region, which represents the pipes, is stamped on the fluid afterwards. Wall thickness is applied as a parameter. The heat transfer by conduction is still represented in lateral directions.

For computation, the finite volume method is used. The conservation equations for mass, momentum and energy are adopted in integral form. For an efficient simulation strategy, the computation domain is divided in three mesh continua. The first mesh continuum contains the frame, sealing and transparent cover and is meshed with the “Thin Mesher”. The “Thin Mesher” generates a prismatic type volume mesh for thin volumes. The second mesh continuum contains the riser pipes. The riser pipes are meshed with the “Direct Mesher”. This method generates a high quality mesh and is flow-aligned in the present case. The third mesh continua includes the air volume, the thermal insulation and the collecting pipes and is meshed with the “Polyhedral Mesher”. In fluid regions, prism layers are used to solve the boundary layer. The mesh consist of 7.8 Mio cells in total.

4. Radiation

To model energy transfer by means of radiation a radiation model as well as a radiation spectrum model is needed. The Surface-to-Surface (S2S) model is used as the radiation model. The S2S model considers radiation as an exclusive surface phenomenon. The surface properties are defined with the optical properties absorptance, reflectance and transmittance. Fluids that are present between surfaces are not include in the radiation heat transfer. Therefore, the air in the gap between the absorber and the transparent cover does not absorb, emit or scatter radiation. As dry air is transparent for radiation, this assumption is considered as permitted.

The base of the Surface-to-Surface model is a spatial discretization of the boundary surfaces into contiguous, non-overlapping patches. Then, a specified number of beams is emitted from each patch-center over the enclosing hemisphere with solid angles. Every beam is traced through the computational domain until it meets another patch. Between these pairs of patches, radiation energy is exchanged. The amount of radiation energy transferred is calculated from the boundary conditions and the radiation transport equation.

The optical properties absorption (α), reflection (ρ) and transmission (τ) are spectral directional quantities. That means that they are dependent on wavelength (λ) and the direction of incoming radiation. From Kirchhoff's law, the spectral directional emittance is, for the same wavelength, equal to the spectral directional absorptance. In STAR-CCM+, directional properties are not applied. Kirchhoff's law is implemented as Eq. 2 for the Multiband Thermal Radiation model and as Eq. 3 for the Gray Thermal Radiation model.

$$\varepsilon_\lambda = \alpha_\lambda \qquad \text{Eq. 2}$$

$$\varepsilon = \alpha \qquad \text{Eq. 3}$$

Essential components of a flat plate collector are the absorber and the transparent cover. Today absorber plates are usually selective coated. The coating leads to a high absorptance of up to $\alpha_{sol} = 0.95$ for radiation with short wavelengths (solar irradiation) and low emittance down to $\varepsilon_{100°C} = 0.05$ for radiation with long wavelengths (thermal radiation). High sensitivity on wavelength also occurs on optical properties for glass plates. Glass plates used for flat plate collectors have a transmittance of 0.9 and higher in the range of solar irradiation, whereas they are almost opaque in the range of infrared radiation. This reveals that a wavelength dependent radiation spectrum model is necessary. To accommodate the wavelength dependency of the optical properties of the surfaces, the Multiband Thermal Radiation model is implemented. Specifying numerous wavelength bands is possible. Optical properties of surfaces are then defined for each wavelength band. During the solution process, the governing radiation equations are solved for each band. The total radiation solution is obtained by summing up the solutions from each band. Because the governing equations are solved for each band, the computing time generally increases with the number of bands. Two spectral bands were defined, one for solar irradiation (short wavelength) and one for infrared radiation (long wavelength). For simulations, wavelength

dependent optical properties were partly taken from literature and partly from measurements performed with an UV-VIS-NIR spectrometer for solar spectrum and an emission meter at 70 °C sample temperature for infrared radiation. Tab. 2 displays the absorptance and accordingly emittance and transmittance for the components pictured in Fig. 3. The reflectivity of the materials was calculated using Eq. 4 for transparent materials and Eq. 5 for opaque materials.

Tab. 2: Optical properties of the different collector components

-	absorptance / emittance		transmittance	
Spectral band	short	long	short	long
Absorber plate	0.95	0.05	-	-
Transparent cover	0.02	0.88	0.91	0.0
Frame	0.2	0.01	-	-
Sealing	0.95	0.91	-	-
Thermal insulation	0.5	0.5	-	-
Absorber pipes	0.3	0.3	-	-

$$\alpha + \rho + \tau = 1 \qquad \text{Eq. 4}$$

$$\alpha + \rho = 1 \qquad \text{Eq. 5}$$

5. Heat Conduction in thermal insulation material

Thermal losses through heat conduction mainly take place through the thermal insulation on the backside of the absorber. Heat transfer through a porous material, as a thermal insulation, is a result from thermal radiation and thermal conduction as well as their interaction with mass transfer in humid materials. According to **Krischer and Kast (1963)**, convection affects the heat transfer only when an air layer becomes 1 cm or thicker. Based on thermal conductivity and thermal radiation, Krischer and Kast introduced a model for mapping thermal conductivity as a function of temperature for porous materials. As for thermal radiation, temperature affects heat transfer with the power of 4, effective thermal conductivity of a thermal insulation increases exponentially with increasing temperature. However, in the range that is relevant for flat plate collectors, with average temperatures of about 150 °C, the thermal conductivity can be modelled with a linear equation as a function of temperature **(Vetter et al. 2015)**.

For the implementation in the CFD simulation, the linear equation for effective thermal conductivity of a sample thermal insulation was determined. Therefore, the thermal conductivity was measured at five average temperatures between 10 °C and 90 °C by means of a Two-Plate-Apparatus. The values of Eq. 6 were then determined by linear regression from the measured data. Information about test method, modeling according to Krischer and Kast and simplified mapping is given in **Vetter et al. (2015)**.

$$k = 0.032 + 0.0023 * \vartheta \qquad \text{Eq. 6}$$

with:

k	thermal conductivity	[W/(m K)]
ϑ	temperature	[°C]

Fig. 4 shows the temperature distribution of the thermal insulation material at the surface towards the absorber at an averaged fluid temperature of 63 °C. Surface temperatures from approximately 40 °C to 90 °C occur. On the backside interface, between thermal insulation and frame, temperatures between 27 °C and 34 °C appear. In this temperature range the thermal conductivity is larger than the value stated in the manufacturer's data sheet, which is normally related to a mean temperature of 10 °C. In the present case, the thermal conductivity of the thermal insulation from the data sheet is $\lambda \leq 0.035$ W/(m K). Tab. 3 lists the minimum, maximum and volume averaged thermal conductivity relating to volume averaged fluid temperature. At an averaged fluid temperature of 81 °C, maximum thermal conductivity exceeds the value from the data sheet by more than 50 %. Even volume averaged thermal conductivity exceeds this value by more than 30 %. As thermal conductivity of

thermal insulations is strongly dependent on temperature, values from the manufacturer data sheet at 10 °C should neither be used for virtual collector testing nor for designing collectors.

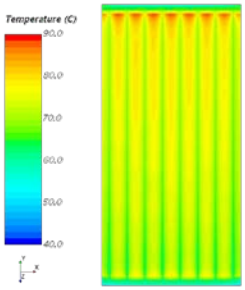

Fig. 4: Temperature distribution of the absorber oriented surface of the thermal insulation.

Tab. 3: Thermal conductivity of thermal insulation relating to volume averaged fluid temperature.

Volume averaged fluid temperature [°C]	**23.7**	**44.0**	**63.0**	**81.1**
Minimum thermal conductivity [W/(m² K)]	0.037	0.038	0.039	0.039
Maximum thermal conductivity [W/(m² K)]	0.045	0.049	0.052	0.055
Volume averaged thermal conductivity [W/(m² K)]	0.039	0.042	0.044	0.046

6. Fluid flow in absorber pipes

In compliance with DIN EN ISO 9806 virtual collector performance test is done with water as a heat transfer fluid in the absorber pipes. Fluid properties are temperature dependent and were implemented as equations, determined from property value tables from **VDI Heat Atlas (2013)**. Temperature dependent equations for dynamic viscosity, density, specific heat and thermal conductivity were embedded.

An important dimensionless parameter for viscous flow is the Reynolds (Re) Number. Re Number is defined by Eq. 7. For pipes with circular cross-section Eq. 8 is also valid. If Re < 2300, flow is laminar, if Re >4000 flow is turbulent. In between is a transition zone, flow can be either laminar or turbulent or a mixture of both.

$$Re = \frac{\rho v D}{\mu} = \frac{v D}{\nu} \qquad \text{Eq. 7}$$

$$Re = \frac{4\dot{V}}{\pi D \upsilon} = \frac{4\dot{m}}{\pi D \mu} \qquad \text{Eq. 8}$$

Where ρ is the density [kg/m³], v is the average fluid velocity [m/s], D is the pipe diameter [m], μ is the dynamic viscosity [m²/s], υ is the kinematic viscosity [Pa s], $\dot{V}$ is the volume flow rate [m³/s] and $\dot{m}$ is the mass flow rate [kg/s].

It can be shown, that the flow pattern of a fully developed laminar flow in a pipe is parabolic. Averaged velocity is half of maximal velocity (= velocity in centerline). Depending on Re Number and diameter, laminar flow is fully developed after entrance length (l_e). Entrance length is calculated according to Eq. 9.

$$l_e = 0.06 * Re * D \qquad \text{Eq. 9}$$

Due to pressure drop, the mass flow rates in the different riser pipes are not exactly the same. Hereafter riser pipe 5 (from the left) is analyzed, Tab. 4. Other raising pipes show similar results.

Tab. 4: Volume averaged temperature, mass flow rate, Re Number and entrance length of riser pipe 5

Volume averaged temperature [°C]	mass flow rate [kg/s]	Re (Eq. 7)	Re 3 (Eq. 8)	entrance length [m]
24.5	0.0052	1409	1412	0.44
44.8	0.0052	2124	2129	0.67
63.6	0.0053	2892	2899	0.91
81.6	0.0053	3694	3702	1.16

Re number according to Eq. 7 and Eq. 8 differ less than 0.3 %. As Re < 4000 for all temperatures, flow was defined as laminar. The entrance length was verified by means of CFD simulations for both constant

temperatures and during the virtual performance test. After entrance length, the requirement that average velocity is half of maximum velocity is fulfilled, with a deviation of less than 2 %.

7. Convective heat loss to the environment

According to **DIN EN ISO 9806** air with a speed of 3 ± 1 m/s has to flow parallel to the collector outer surfaces during the performance test. In general, there are two possibilities to transfer this requirement to CFD simulations. The first is to establish an air volume around the collector with the enforced wind speed. The disadvantage is again that the mesh would contain a huge number of cells. To avoid the need of the air volume around the collector a convective heat transfer coefficient is implemented as boundary condition.

Literature shows a wide range of heat transfer coefficients for forced air flow over flat surfaces or particularly flat plate collectors. On the one hand are empirical equations and on the other hand equations from boundary layer theory. **Sartori (2006)** gives an overview. Following some equations are shown and compared.

Eq. 10 was implemented by **Jurges (1924)** for a vertical surface of 0.5 m x 0.5 m and is widely used for flat plate collectors.

$$h_c = 5.7 + 3.8 * v \quad \text{Eq. 10}$$

with:

h_c	heat transfer coefficient	[W/(m² K)]
v	wind velocity	[m/s]

Watmuff et all. (1977) suggested that Eq. 10 presumably comprises radiative effects and recommended Eq. 11.

$$h_c = 2.8 + 3.0 * v \quad \text{Eq. 11}$$

Lunde (1980) suggested Eq. 12.

$$h_c = 4.5 + 2.9 * v \quad \text{Eq. 12}$$

Boundary layer theory leads to Eq. 13 for laminar flow and Eq. 14 for fully turbulent flow. Both, Eq. 13 and Eq. 14 were developed for flat surfaces and constant surface temperatures.

$$Nu = 0.664 * Re^{0.5} * Pr^{\frac{1}{3}} \quad \text{Eq. 13}$$

$$Nu = 0.0369 * Re^{0.8} * Pr^{\frac{1}{3}} \quad \text{Eq. 14}$$

Incorpera and deWitt (1985) remark that it is fundamental for every convection problem to first determine, whether the boundary layer is laminar or turbulent. The heat loss strongly depends on which of these conditions occur. The empirical equations Eq. 10 to Eq. 12 do not comply with this requirement. **Incorpera and deWitt (1985)** also state, "it´s well known that even small disturbance causes the flow to be turbulent." **Francey and Papaioannou (1985)** do confirm this when they say: "the finite thickness of the collector presents a blunt leading edge to the wind and presumably produce turbulent flow over the surface." Based on **Rowley et al. (1930)** who state that the effect resulting from differing reference temperatures on the convective heat transfer coefficient is not significant, **Sartori (2006)** developed Eq. 15 with a reference temperature of $\vartheta_{ref} = 40\ °C$ for fully turbulent flow over a flat surface. L is the flat plate length in wind direction.

$$h_c = 5.74 * v^{0.8} * L^{-0.2} \quad \text{Eq. 15}$$

Fig. 5 shows the convective heat transfer coefficient from Eq. 10 to Eq. 12 and Eq. 15 as a function of wind speed. As Eq. 10 presumably includes radiative effects, the convective heat transfer coefficient according to wind speed displays the highest values. Empirical Eq. 11 and Eq. 15 derived from boundary layer theory demonstrate a good match. Eq. 12 is in between.

According to boundary layer theory, the convective heat transfer is both, dependent on wind speed and the length of the flat plate in wind direction. The decay is proportional to $L^{-0.2}$ for turbulent flows, and to $L^{-0.5}$ for laminar flows. Experimental results from **Parmelee and Huebscher (1947)** and **Test et al. (1981)** found again, that the average convective heat transfer coefficient of a flat plate decreases with increasing length. Fig. 6 shows the convective heat transfer coefficient as a function of the surface length in wind direction, calculated from Eq.

10 to Eq. 12 and Eq. 15. Compared to Eq. 15, empirical equations Eq. 10 to Eq. 12 do not consider the decay of the convective heat transfer coefficient with increasing surface length in wind direction.

As the objective of this work is a development and optimization tool for flat plate collectors, which could be a modification of the length in wind direction, Eq. 15 is implemented as a boundary condition for all outer surfaces of the collector. Technically speaking Eq. 15 is not valid for the front ends, but as the convective heat loss is small over the front ends, the error is marginal.

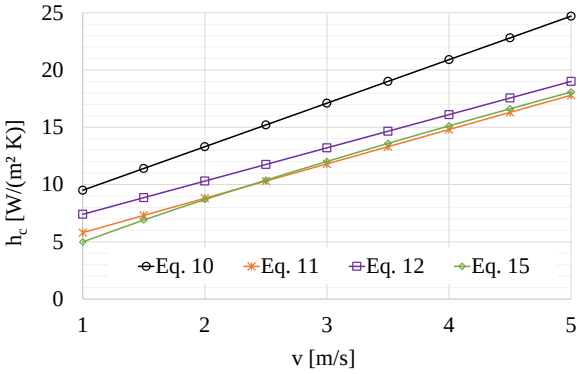

Fig. 5: Convective heat transfer coefficient as a function of wind speed

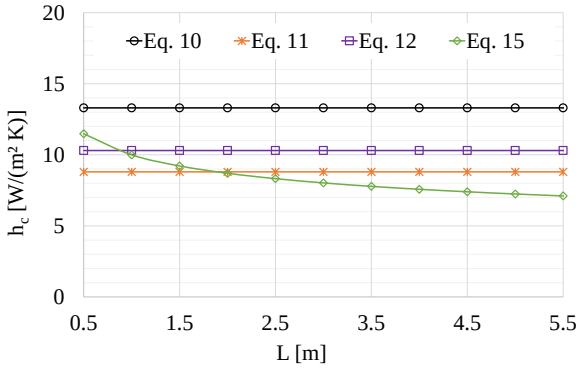

Fig. 6: Convective heat transfer coefficient as a function of surface length in wind direction

8. Virtual collector performance test

A virtual collector performance test was conducted. In order to validate the results determined by the virtual collector performance test, component temperatures were measured during a real physical performance test of collector C1375 in a solar simulator and the boundary conditions from this measurement were implemented in CFD simulations, compare Tab. 1. Wind velocity is measured during the thermal performance test at a corner of the collector. The measurement of the wind velocity during the test is not representing to 100 % the wind velocity on all outer surfaces of the collector. To study the influence of wind velocity, virtual thermal performance tests have been executed for 2 m/s (measured at indoor test of collector C1375) and for 3 m/s (measured at outdoor test of collector C1373), respectively h_c = 8.7 W/(m² K) and h_c = 12 W/(m K), acc. Eq. 15.

Fig. 7 and Fig. 8 show some of the points of temperature measurement. Temperature measurements have been executed using thermocouples. They were mounted on the backside of the absorber and on the inside of the frame.

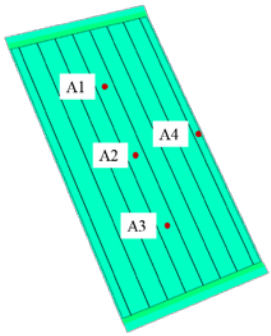

Fig. 7: Points of temperature measurement on the backside of the absorber

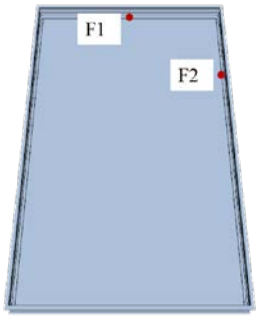

Fig. 8: Points of temperature measurement on the inside surface of the frame

Tab. 5 displays a comparison between measured and simulated outlet- and component temperatures for convective heat transfer coefficients at the outer collector surfaces of h_c = 8.7 W/(m² K) and h_c = 12 W/(m² K). The maximum deviation for component temperatures is -3.7 K at point A1 for h_c = 8.7 W/(m² K) and ϑ_{in} = 79 °C (simulated absorber temperature is 3.7 K higher than measured). The simulation for the same set of boundary conditions also shows the maximum deviation in the simulated outlet temperature. While temperature difference

between in- and outlet measured accounts for 3.14 K, the temperature difference resulting from the simulation is 3.79 K. Therefore, the outlet temperature in simulation shows a 0.65 K higher temperature increase than measured. As also shown in chapter 2, measurement results between indoor measurement of C1373 and C1375 as well as outdoor measurement of C1373 show differences.

Tab. 5: Comparison between measurement and simulation results

ϑ_{in} = 19.9 °C	**-**	**h_c = 8.7 W/(m² K)**		**h_c = 12 W/(m² K)**	
	Measured [°C]	**Simulated [°C]**	**Difference [K]**	**Simulated [°C]**	**Difference [K]**
ϑ_{out} - ϑ_{in} [K]	6.45	6.18	0.27	6.15	0.3
A1	43.8	43.9	-0.1	43.8	0.0
A2	43.2	42.0	1.2	41.9	1.3
A3	41.3	39.5	1.8	39.5	1.8
A4	41.7	39.3	2.4	39.2	2.5
F1	27.5	26.6	0.9	25.6	1.9
F2	25.9	25.0	0.9	24.3	1.6
ϑ_{in} = 40.8 °C	**-**	**h_c = 8.7 W/(m² K)**		**h_c = 12 W/(m² K)**	
	Measured [°C]	**Simulated [°C]**	**Difference [K]**	**Simulated [°C]**	**Difference [K]**
ϑ_{out} - ϑ_{in} [K]	5.22	5.42	-0.2	5.35	-0.13
A1	60.6	61.9	-1.3	61.6	-1.0
A2	60.2	60.1	0.1	60.0	0.2
A3	58.8	57.7	1.1	57.5	1.3
A4	58.3	56.4	1.9	56.2	2.1
F1	29.1	29.5	-0.4	27.9	1.2
F2	27.8	27.6	0.2	26.3	1.5
ϑ_{in} = 60.3 °C	**-**	**h_c = 8.7 W/(m² K)**		**h_c = 12 W/(m² K)**	
	Measured [°C]	**Simulated [°C]**	**Difference [K]**	**Simulated [°C]**	**Difference [K]**
ϑ_{out} - ϑ_{in} [K]	4.26	4.61	-0.35	4.52	-0.26
A1	75.3	78.3	-3.0	78.0	-2.7
A2	74.7	77.1	-2.4	76.6	-1.9
A3	73.7	74.8	-1.1	74.7	-1.0
A4	71.9	72.2	-0.3	71.8	0.1
F1	30.9	32.6	-1.7	30.2	0.7
F2	29.9	30.5	-0.6	28.4	1.5
ϑ_{in} = 79.0 °C	**-**	**h_c = 8.7 W/(m² K)**		**h_c = 12 W/(m² K)**	
	Measured [°C]	**Simulated [°C]**	**Difference [K]**	**Simulated [°C]**	**Difference [K]**
ϑ_{out} - ϑ_{in} [K]	3.14	3.79	-0.65	3.64	-0.5
A1	90.9	94.6	-3.7	93.9	-3.0
A2	90.5	93.1	-2.6	92.7	-2.2
A3	89.7	91.4	-1.7	90.9	-1.2
A4	87.4	87.5	-0.1	87.2	0.2
F1	32.5	35.6	-3.1	32.5	0.0
F2	31.8	33.2	-1.4	30.5	1.3

Fig. 9 illustrates the efficiency curves. Both simulations match η_0 from the outdoor test very well. Because the solar simulator does not match the solar spectrum of the sun to 100 %, η_0 measurement from outdoor tests are

favored. For higher temperature differences, simulations show an increasing deviation compared to experimental performance tests, whereby deviations are smaller for simulations with h_c = 12 W/(m² K).

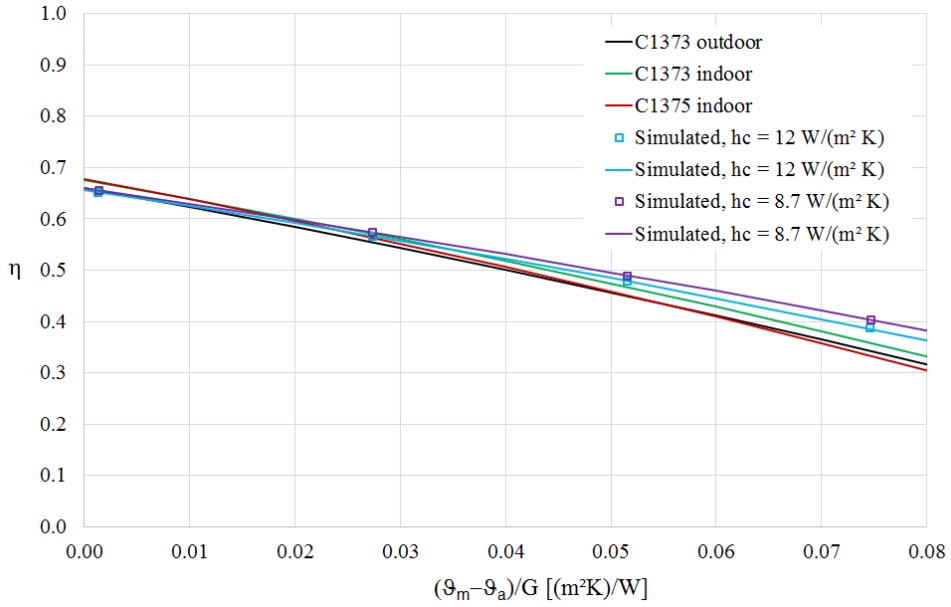

Fig. 9: Efficiency curves, based on experimental data and virtual thermal performance test results (indicated as simulated)

8.1 Annual collector output calculation

To compare the different results on the basis of the annual collector output the calculation tool ScenoCalc (Solar Collector Energy Output Calculator) was used. ScenoCalc is used for in the context of Solar Keymark certification. For all annual collector output calculations the incidence angle modifiers of the outdoor measurement of collector C1373 was used.

Tab. 6: Annual collector output for location Würzburg. Comparison between experimental performance test and simulation with h_c = 8.7 W/(m² K)

ϑ_m [°C]	25	50	75
C1373 indoor [kWh/a]	1329	825	465
Simulation [kWh/a]	1334	894	564
Difference [kWh]	-5	-69	-99
C1375 indoor [kWh]	1312	782	418
Simulation [kWh]	1334	894	564
Difference [kWh]	-22	-112	-146

Tab. 7: Annual collector output for location Würzburg. Comparison between experimental performance test and simulation with h_c = 12 W/(m² K)

ϑ_m [°C]	25	50	75
C1373 indoor [kWh/a]	1329	825	465
Simulation [kWh/a]	1319	866	527
Difference [kWh]	10	-41	-62
C1375 indoor [kWh]	1312	782	418
Simulation [kWh]	1319	866	527
Difference [kWh]	-7	-84	-109

Tab. 6 presents the comparison between the annual collector output derived from experimental performance tests and simulations with h_c = 8.7 W/(m² K) for different mean fluid temperatures ϑ_m. Tab. 7 presents the comparison between the annual collector output derived from experimental performance tests and simulations with h_c = 12 W/(m² K), also for different mean fluid temperatures ϑ_m. Good agreement between annual collector output, calculated from experimental performance test results and from virtual performance test results, are shown for ϑ_m = 25 °C, for both simulations. For rising mean fluid temperatures, deviation increases, compare Tab. 7 and Tab. 6.

8.2 Influence of optical absorber properties

In the manufacturer data sheet of the absorber coating, optical properties are given as follows:

$\alpha_s = 0.95 \pm 0.01$ [-]
$\varepsilon_{100\,°C} = 0.05 \pm 0.02$ [-]

To study the influence of the optical absorber properties, the tolerances given by the manufacturer data sheet were implemented in the CFD model and simulations for an inlet temperature of 79 °C were performed. Tab. 8 presents the results. Maximal influence between $\alpha_{sol} = 0.95$; $\varepsilon_{100\,°C} = 0.05$ and $\alpha_{sol} = 0.94$; $\varepsilon_{100\,°C} = 0.07$ is 0.12 K for simulations with $h_c = 8.7$ W/(m² K), respectively 0.11 K for simulations with $h_c = 12$ W/(m² K). Therefore, tolerances do influence the result, but they do not explain the entire deviation between measurement and simulation at increasing mean temperatures.

Tab. 8: Edge case consideration for optical absorber properties at ϑ_{in} = 79 °C

h_c = 8.7 W/(m² K)		**$\vartheta_{out} - \vartheta_{in}$ [K]**	**h_c = 12 W/(m² K)**		**$\vartheta_{out} - \vartheta_{in}$ [K]**
S1	$\alpha_{sol} = 0.95$; $\varepsilon_{100\,°C} = 0.05$	3.79	S5	$\alpha_{sol} = 0.95$; $\varepsilon_{100\,°C} = 0.05$	3.64
S2	$\alpha_{sol} = 0.95$; $\varepsilon_{100\,°C} = 0.07$	3.72	S6	$\alpha_{sol} = 0.95$; $\varepsilon_{100\,°C} = 0.07$	3.58
S3	$\alpha_{sol} = 0.94$; $\varepsilon_{100\,°C} = 0.05$	3.73	S7	$\alpha_{sol} = 0.94$; $\varepsilon_{100\,°C} = 0.05$	3.60
S4	$\alpha_{sol} = 0.94$; $\varepsilon_{100\,°C} = 0.07$	3.67	S8	$\alpha_{sol} = 0.94$; $\varepsilon_{100\,°C} = 0.07$	3.53
S1 – S4	Maximal deviation	0.12	S5 – S8	Maximal deviation	0.11

8.3 Thermal bridges

CAD buildup contains some simplifications. At the absorber for example, is a temperature sensor socket mounted, which was not reproduced in CAD buildup. Furthermore, the exact position of the absorber in the frame while testing cannot be exactly determined. Due to extension because of temperature, absorber plate can corrugate and therefore contact a fillet which is part of the frame. Former simulations without the fillet have already demonstrated an influence on thermal performance even though no direct contact between absorber and frame persists in the presented simulations.

8.4 Convection in the air gap between absorber and transparent cover

Another factor that may falsify the simulation is the convection in the air gap between absorber and glass plate. However, a detailed analyses about the air flow in the collector is not performed up to now.

9. Conclusion and outlook

An effective simulation strategy was developed for a virtual, CFD based collector test. It was conducted for a serial product flat plate collector. Validation has been executed by comparison of component temperatures, collector efficiency and annual collector output determined based on real physical collector tests and on simulation data. Simulated component temperatures correspond well to measured values. The peak collector efficiency from the virtual thermal performance test fits the result from experimental thermal performance test very well. With increasing mean fluid temperature, the difference between measured and simulated outlet temperature rises. Possible reasons are identified, but need to be analyzed further. The next step is to analyze the air flow in the collector and therefore the convection in the air gap between absorber and glass plate. The authors are confident that appropriate modifications of the CFD simulation model will result in an even better match between the results derived from CFD based virtual collector tests and real physical tests, especially for high mean collector fluid temperatures.

Beate Vetter

10. Acknowledgments

The activities described in this contribution are being supported by the German Federal Ministry for Economic Affairs and Energy (BMWi) based on a decision of the German Bundestag by Projektträger Jülich (PtJ) under grant numbers 0325556 A, Project “VirtColl+ - Entwicklung eines neuartigen, auf CFD Simulationen und virtuellen Kollektorprüfungen basierenden Entwicklungs- und Optimierungswerkzeug für Flachkollektoren / development and optimization tool for flat plate collectors based on CFD simulations and virtual collector performance tests”. The authors gratefully acknowledge this support and carry the full responsibility for the content of this contribution.

11. References

DIN EN ISO 9806:2014-06, Solar energy - Solar thermal collectors - Test methods.

Francey, J.L.A., Paraioannou, J.: Wind-related heat losses of a flat-plate collector. Solar Energy, Bd. 35, Nr. 1, S. 15–19, DOI 10.1016/0038-092X(85)90032-5, 1985.

Incropera, F. P., DeWitt, D. P.: Fundamentals of heat and mass transfer. 2. Aufl., XXIII, 802 S, ISBN 0-471-88550-9, Wiley: New York NY u.a., 1985.

Jürges W. Gesundheitsingenieur, Reihe 1, Beiheft 19, 1924.

Krischer, O., Kast, W.: Die wissenschaftlichen Grundlagen der Trocknungstechnik. Trocknungstechnik, Band 1 ED. 3 REPRINT, XXI, 494 S ;, ISBN 3-540-08280-8, Springer: Berlin [etc.], op. 1992.

Lunde P. J.: Solar Thermal Engineering, Space Heating and Hot Watersystems. John Wiley & Sons Ltd: New York (N.Y.), 1980.

Parmelee, G. V., Huebscher, R. G.: Forced convection heat transfer from flat surfaces, Part 1: smooth surfaces. American Society of Heating and Ventilating Engineers. Research Bulletin, vol. 53, no. 3, November, 1947, 47 S., American Society of Heating and Ventilating Engineers: New York (N.Y.), 1948.

Rowley, F.P., Algren, A.B. Blackshaw, J.L., 1930. Effects of air velocity on surface coefficients. ASHRAE 36, 123-136

Sartori, E.: Convection coefficient equations for forced air flow over flat surfaces. Solar Energy, Bd. 80, Nr. 9, S. 1063–1071, DOI 10.1016/j.solener.2005.11.001, 2006.

Test F.L., Lessmann R.C., Johary A.: Heat Transfer During Wind Flow over Rectangular Bodies in the Natural Environment. ASME J. Heat Transfer.

http://asmedigitalcollection.asme.org/solr/searchresults.aspx?q=heat%20transfer%20during%20wind%20flow%20over%20rectangular%20bodies%20in%20the%20natural%20environment&allJournals=1&f_ContentType=Journals&SearchSourceType=3

VDI-Wärmeatlas. VDI-Buch, 11. Aufl., 1650 Seiten, ISBN 978-3-642-19982-0, Springer Vieweg: Berlin, 2013.

Vetter B., Kofler P., Fischer S., Drück H.: Bestimmung der effektiven Wärmeleitfähigkeit von Wärmedämmmaterialien für Sonnenkollektoren, Tagungsband zum 25. Symposium Thermische Solarenergie, Bad Staffelstein, Kloster Banz, Deutschland, ISBN 978-3-3943891-51-5

Watmuff, J.H. and W.W.S. Proctor D.: Solar and wind conducted external coefficients for solar collectors. 1977. https://www.researchgate.net/publication/234355019_Solar_and_wind_induced_external_coefficients_-_Solar_collectors